Available online at www.sciencedirect.com
ScienceDirect
Trans. Nonferrous Met. Soc. China 33(2023) 2926−2942
Transactions of Nonferrous Metals Society of China
www.tnmsc.cn

Multi-scale simulation of flow behavior and microstructure evolution for AA2219 alloy during multi-pass ring rolling process

Fang DONG[1,2], Tao ZHANG[1,2], Yun-xin WU[1,2], Lei LIU[1,2], Tie-wen HAO[1,2,3]

1. Light Alloy Research Institute, Central South University, Changsha 410083, China;
2. State Key Laboratory of High-Performance Complex Manufacturing, Central South University, Changsha 410083, China;
3. Dalian Engineering Technology Co., Ltd., China First Heavy Industries, Dalian 116600, China

Received 2 April 2022; accepted 17 August 2022

Abstract: The multi-scale simulation of flow behavior and microstructure evolution of 2219 aluminum alloy during ring rolling was conducted. A new forming technology with two-stage hot−warm ring rolling was proposed compared to conventional hot rolling. The results show that the distributions of temperature, strain and strain rate are inhomogeneous on the cross section. The grains of edge nodes are elongated resulting from the larger strain and the low-angle grain boundaries transform into high-angle grain boundaries resulting in the increased fraction of recrystallization in hot rolling. The elongated banded structures change to equiaxed grains during the solution treatment, indicating complete static recrystallization. The inhomogeneous distributions of the temperature and strain result in heterogeneous microstructure distribution. The rolling force and the geometry of the ring were analyzed with experiment. The tensile properties in all directions of the ring and its isotropy are significantly increased with the new technology, especially the elongation.

Key words: 2219 aluminum alloy; two-stage hot−warm ring rolling; microstructure simulation; recrystallization; tensile properties

1 Introduction

2219 aluminum alloy (AA2219), with comprehensive advantages of light weight, high strength and ductility, good weldability and resistance in high and low temperatures [1], was widely used in the aerospace industry, such as the rocket propellant tank transition ring [2].

With the development of the aerospace industry, the ring with larger size and much higher requirements of the comprehensive properties is highly required. The maximum outside diameter of the ring is over 10 m and its mechanical properties are much higher than those of the current *d*5 m ring [3].

The transition ring is mainly manufactured by the radial−axial rolling of ring blank [4]. A conventional process of ring rolling of AA2219 is that the ring blank is hot rolled at 460 °C with 50% deformation followed by the solution and aging treatment. The hot ring rolling process with large deformation can result in inhomogeneous deformation in each direction, causing low ductility and significant anisotropy in the large rings [5]. Additionally, dynamic recovery is easily initiated during the hot forming process (400−520 °C), and dynamic recrystallization may even occur when the deformation reaches the critical strain [6]. This leads to a low static recrystallization nucleation rate in the subsequent solution treatment, and ultimately a coarse and heterogeneous grain structure. Low ductility has become the main problem restricting the application of the large connect ring [7].

Corresponding author: Tao ZHANG, Tel: +86-15274969416, E-mail: larizhangtao@csu.edu.cn
DOI: 10.1016/S1003-6326(23)66308-3

In summary, the flow behavior, microstructure evolution and its significant anisotropy of the ring during the multi-pass ring rolling are quite complex [8,9]. The grain refinement of 2219 aluminum alloy cannot be achieved by hot deformation and solution treatment. Therefore, the warm rolling process is investigated in this study and its effect on the microstructure evolution and mechanical properties is analyzed.

Finite element models (FEM) were widely used for the macroscopic simulation of ring rolling process [10]. Cellular automata (CA) models had been proposed for the microstructure simulation of forming process on the basis of principles of physical metallurgy and mathematical stochastic algorithm [11]. The mechanical properties of the ring were related to the microstructure, which was affected by the forming parameters during the multi-pass ring rolling processes. It was imperative to develop the multi-scale simulation of AA2219 ring rolling process to explore the synergistic control scheme of steady forming and micro-structure evolution.

Many previously published works have been focused on the flow behavior of the ring rolling process [12]. HAN et al [13,14] studied the influence of friction coefficient and axial/ circumferential rolling ratio on the metal flow of the thin-walled cylindrical ring with FEM. ZHU et al [15] improved a 3D thermo-mechanical coupled FEM of ring rolling process using the response surface method to optimize the cooperative feed strategy. LIANG et al [16] developed an intelligent real-timely force-controlled FEM and the rolling path can be automatically adjusted in a real-time manner to satisfy the control target of the rolling force. This work achieved quick planning of the rolling path which not only satisfied but also adequately utilized the rolling force limit.

The microstructure evolution during multi-pass ring rolling processes was quite complex and it was affected by the forming parameters. The experiments of the microstructure can be only used to reveal the microstructure characteristic of some key positions of the ring or at some specific stages. CA models were widely used to simulate the microstructure variation induced by the dynamic recrystallization (DRX) [17], the meta-dynamic recrystallization (MDRX) [18], the static recrystallization (SRX) [19] and the thermo-mechanical treatment (TMT) process [20]. BAKHTIARI and SALFHI [21] improved the microscopic scale simulation by using the normal growth, topological deformation and texture reconstruction techniques. LEE and IM [22] established an improved cellular automata model by incorporating a new parameter to take solute resistance effect into consideration. JIN et al [23] proposed a nucleation parameter identification method by the flow stress curves and improved a CA model for DRX simulation.

Multi-scale simulation under different thermal processing methods had also been carried out [24]. ZHANG et al [25] established coupled FEM−CA models to compare strain and temperature characteristics and microstructure evolution during multi-pass rolling of the symmetrical rolling and asymmetrical shear rolling. ZHENG et al [26] established CA models to predict microstructure variation of different recrystallization during multi-pass symmetrical rolling. It enabled both quantitative and topographic prediction of the microstructural evolution during industrial hot-rolling processing.

The preparation of the final ring component from the ring blank consisted of multi-pass ring rolling and the followed heat treatment. The flow behavior of the strain and temperature was quite complex, inducing complicated microstructure evolution of the ring. Previously published works were mainly focused on the conventional hot ring rolling process of the metal alloy.

In this study, a novel forming technology with two-stage hot and warm ring rolling process was proposed for AA2219 ring. A coupled FEM−CA model was established to investigate the flow behavior and the microstructure evolution in different positions of the ring with new forming technology proposed in this study. The results of the ring with conventional hot ring were described as comparisons to those of the ring with new forming technology. The engineering tests of two-stage hot and warm ring rolling were conducted and the geometry, temperature, microstructure and tensile properties of the ring were analyzed in comparison with the simulated results. The conventional hot ring rolling was also conducted and its microstructure and tensile properties were analyzed and compared to those with two-stage hot and warm ring rolling.

2 FEM−CA coupled models

The preparation of the large ring components was quite complex, including the casting, homogenization treatment, hot forging, solution treatment, warm forging, ring rolling and solution-aging treatment. The casting and forging processes were essential for the preparation of the ring blank with high mechanical properties. The ring blank prepared from the forging process was hot rolled into the final ring component with conventional ring forming technology; while a novel technology of two-stage hot−warm ring rolling followed by solution treatment was proposed in this study. This study was focused on the forming processes of the ring component from the ring blank. Work hardening and continuous dynamic recrystallization (CDRX) occurred in the deformation zones during the ring rolling process for AA 2219 alloy; while the static recovery and static recrystallization (SRX) took place during the pass interval time of the multi-pass ring rolling process. Additionally, high temperature solution treatment was adopted immediately after the warm rolling process; the effect of intermediate thermo-mechanical treatment (ITMT) on the microstructure variation should be taken into consideration.

The variation and distribution of the macro parameters (temperature, strain and strain rate) were quite complex during the two-stage hot−warm multi-pass ring rolling process. Meanwhile, the macro parameters played significant roles in the microstructure evolution, thus changing the mechanical properties of the final ring component. In this study, coupled FEM−CA models were established and the distributions of the temperature, strain and strain rate could be obtained using the thermal-mechanical models in FEM. The coupled FEM−CA method of ring rolling process was achieved through the data transmission between the FEM and CA models to achieve the macro and micro cross-scale integrated simulation. The results of the temperature, strain and strain rate of the FEM were input into the CA model as the initial conditions.

2.1 FEM model

3D thermo-mechanical models of ring rolling were established. The material of the ring blank was AA2219 and its flow behavior could be obtained in previously published works [27,28]. The rolls (including the main roll, mandrel, axial roll and guide roll) were defined as rigid bodies with thermal conductivity. The coordinated movements of the mandrel, axial roll and guide roll played a vital role in the stable ring rolling process. The definition of the movement for all rolls needed to be adjusted and controlled in the real-time ring rolling process. Therefore, the coordinated motion control program of stable rolling was developed through the subroutine VUAMP. The dimensions and the speed of the rolls are given in Table 1. The friction coefficient between the ring blank and the rolls was set to be 0.3 for both hot and warm rollings [10]. There were two rolling stages for the preparation of the final ring component, including hot rolling and warm rolling. The initial dimensions of the ring blank were 3000 mm (outer diameter) × 2400 mm (inner diameter) × 300 mm (length) and it was hot rolled into the thickness of 240 mm with the initial temperature of 500 °C, and then it was warm rolled into the thickness of 180 mm with the initial temperature of 250 °C. The temperature of the ring was related to the heat exchange with the contact rolls and environment. The heat transfer coefficient

Table 1 Parameters of ring rolling

Parameter	Value
Main roll radius/mm	665
Mandrel radius/mm	620
Guide roll radius/mm	600
Cone angle of axial roll/(°)	30
Length of axial roll/mm	1280
Outer radius of ring blank/mm	1500
Inner radius of ring blank/mm	1200
Thickness of ring blank/mm	300
Main roll speed/(rad·s^{-1})	1.35
Temperature of rolls/°C	100
Initial temperature/°C	250, 500
Ambient temperature/°C	20
Heat transfer coefficient with rolls/(N·s^{-1}·mm^{-1}·°C^{-1})	10
Heat transfer coefficient with environment/(N·s^{-1}·mm^{-1}·°C^{-1})	0.02
Emissivity	0.7
Friction coefficient	0.3

between the ring and environment and the contact rolls was defined as 0.02 and 10 $N·s^{-1}·mm^{-1}·°C^{-1}$, respectively. The emissivity due to the radiation was 0.7.

2.2 CDRX-CA model

The recrystallization mechanism of AA2219 during hot forming process was CDRX through the high angle grain boundaries (HAGBs) migration and the sub-grain growth. The dislocation density was an important parameter and it increased during the work hardening process and decreased during the dynamic recovery and CDRX processes. Estrin−Mecking models [29] were adopted to describe the variation of dislocation density, as shown in Eqs. (1)−(3). The relationship between the flow stress under different forming parameters and the dislocation density was shown in Eq. (4):

$$d\rho/d\varepsilon=k_1-k_2\rho \tag{1}$$

$$k_1=1/(bl) \tag{2}$$

$$k_1=k_2[\sigma_s/(\alpha Gb)]^2 \tag{3}$$

$$\sigma=\alpha Gb\sqrt{\rho} \tag{4}$$

where ρ is the dislocation density, ε is the true strain, k_1 and k_2 are the coefficients of work hardening and dynamic softening, respectively, b is the magnitude of the Burger vector, l is the mean free path of dislocation, σ_s is the steady flow stress, σ is the flow stress, α is the material constant, and G is the shear modulus.

When the dislocation density reached the critical value, the recrystallized nuclei started to appear. The nucleation rate was related to the temperature and the strain rate based on Guo's model [30], as shown in Eqs. (5) and (6):

$$\rho_c=\left(\frac{20\gamma\dot{\varepsilon}}{3blM\tau^2}\right)^{1/3} \tag{5}$$

$$\dot{n}=C\dot{\varepsilon}^m\exp\left(\frac{Q_c}{RT}\right) \tag{6}$$

where ρ_c is the critical dislocation density, γ is grain boundary energy, $\dot{\varepsilon}$ is the strain rate, M is grain boundary mobility, τ is the dislocation line energy, $\dot{n}$ is the nucleation rate, C and m are constants, Q_c is the nucleation activation energy, T is the temperature, and R is molar gas constant and it equals 8.314 J/(mol·K).

The recrystallized nuclei started to grow and the dislocation density difference between the recrystallized grains and the initial grains provided the driving force for the grains growth. The migration velocity was related to the mobility of the grain boundary and the pressure, and the mobility of the grain boundary changed with the variations of the temperature and the strain rate, as shown in Eqs. (7)−(9):

$$v=Mp \tag{7}$$

$$M=\frac{\delta D_b b}{kT}\dot{\varepsilon}^m\exp\left(-\frac{k_1Q_b}{RT}\right)\left\{1-\exp\left[-5\left(\frac{\theta_i}{\theta_m}\right)^4\right]\right\} \tag{8}$$

$$p=F/(4\pi r^2) \tag{9}$$

where v is the migration velocity, p is the pressure, δ is the characteristic thickness of grain boundary, D_b is the boundary self-diffusion coefficient, Q_b is the boundary diffusion activation energy, k is Boltzmann constant, θ_i is the misorientation between the ith recrystallized grain and its neighboring grain, θ_m is the critical misorientation, F is the driving force, and r is the radius of the grain.

The grains could be elongated in rolling direction and compressed perpendicular to the rolling direction, thus changing the microstructure evolution. The topological deformation model was described in Eq. (10):

$$\begin{pmatrix} m_x \\ m_y \end{pmatrix}=\begin{pmatrix} l_{xx} & 0 \\ 0 & l_{yy} \end{pmatrix}\begin{pmatrix} u_x \\ u_y \end{pmatrix} \tag{10}$$

where u_x and u_y are cell sizes in horizontal and vertical directions before deformation; m_x and m_y are cell sizes after each CA step with rolling deformation. The relationship between ε and l is $\ln l_i=\varepsilon_i$.

2.3 SRX-CA model

During the multi-pass ring rolling process, different mechanisms would occur during the pass interval, such as static recovery and static recrystallization. The dislocation density would decrease at high temperature during the pass interval due to the static recovery, as described in Eq. (11). The exponent of static recovery was 1 at high temperature during the pass interval and the dislocation density decreased due to the dislocation annihilation induced by the motion of sub-boundaries, as shown in Eq. (12):

$$d\rho/dt=-k_s(\rho-\rho_0)^n \tag{11}$$

$$\rho=(\rho_d-\rho_0)\exp(-k_st)+\rho_0 \tag{12}$$

where ρ_0 is the initial dislocation density, t is the pass interval time, n is the exponent of static recovery, ρ_d is the dislocation density immediately after the deformation, and k_s is the coefficient of static recovery.

The nucleation model in SRX could be described in Eq. (6). The mobility of the grain boundary was not related to the variation of the strain rate during the pass interval, and the calculation of the mobility of the grain boundary (M_s) could be described in Eq. (13):

$$M_s=\frac{\delta D_b b}{kT}\exp\left(-\frac{k_2 Q_b}{RT}\right)\left\{1-\exp\left[-5\left(\frac{\theta_i}{\theta_m}\right)^4\right]\right\} \tag{13}$$

2.4 IIMT-CA model

The IIMT consisted of the warm ring rolling and the subsequent high-temperature solution treatment. The deformation energy accumulating in the ring rolling process provided the driving force for the static nucleation during the high-temperature solution treatment; the static nucleation could be described in Eqs. (14) and (15). The parameters of CA models for AA2219 are given in Table 2.

$$\dot{n}_s=\alpha_0\left(E-E_c\right)\exp\left(\frac{-Q_N}{RT_s}\right) \tag{14}$$

$$E=cG\rho b^2 \tag{15}$$

where $\dot{n}_s$ is the nucleation ratio, α_0 is the material constant, E is the deformation energy, E_c is the critical deformation energy, Q_N is the thermal activation energy of nucleation, T_s is the solution temperature and it is set to be 813 K in this study, and c is the material constant.

Table 2 Parameters of CA models

Parameter	Value
Material constant, α	0.5
Shear modulus, G/GPa	26
Nucleation constant, C	1.817
Nucleation constant, m	−0.085
Nucleation activation energy, Q_c/(J·mol^{-1})	1299
Thickness of grain boundary, δ/m	2.1×10^{-7}
Boundary self-diffusion coefficient, D_b/(m^2·s^{-1})	1.7×10^{-4}
Boundary diffusion activation energy, Q_b/(J·mol^{-1})	1.42×10^{5}
Boltzmann constant, k/(J·K^{-1})	1.38×10^{-23}
Critical misorientation, θ_m/(°)	15
Exponent of static recovery, n	1

3 Results and discussion

3.1 Hot ring rolling in new forming process

3.1.1 Flow behavior analysis with FEM

The distribution of the temperature is inhomogeneous and five nodes in the cross section of the ring are analyzed, as shown in Fig. 1. The overall temperature of the cross section decreases with the proceeding of the ring rolling process. The core temperature is much higher than that on the edges of the cross section, and the largest temperature drop occurs at Node 1 on the top surface, while the smallest temperature drop appears at Node 3. The temperature distribution is affected by the plastic heat production and the heat dissipation, including heat conduction, heat convection and heat radiation. The heat dissipation due to the heat exchange between the ring blank and the rolls as well as the environment is much larger than the heat production induced by the plastic deformation, as can be seen from the decrease of overall temperature in the cross section. The temperature drop at Node 1 is larger than that at Node 2 and Node 3. There is obvious deformation at Node 2 and Node 3 in the rolling deformation zone due to the significant pressure between the edge surfaces of the ring and the work rolls. The temperature increase due to the plastic heat production will compensate for the temperature drop at Node 2 and Node 3 compared to that of Node 1. Additionally, the temperature at edge surfaces of the ring cross section decreases with fluctuation with the proceeding of the rolling process, while the temperature at center part declines continuously. There is heat exchange between the edge surfaces of the ring and the work rolls, which decreases the temperature. Meanwhile, the heat conduction between the center part and the edge surfaces of the ring occurs due to the higher temperature in the center part, thus increasing the temperature of the edge surfaces instantaneously. As a result, the temperature of the edge surfaces shows repeated fluctuation during the multi-pass ring rolling process. The temperature drop at center part increases with the increased rolling pass. The

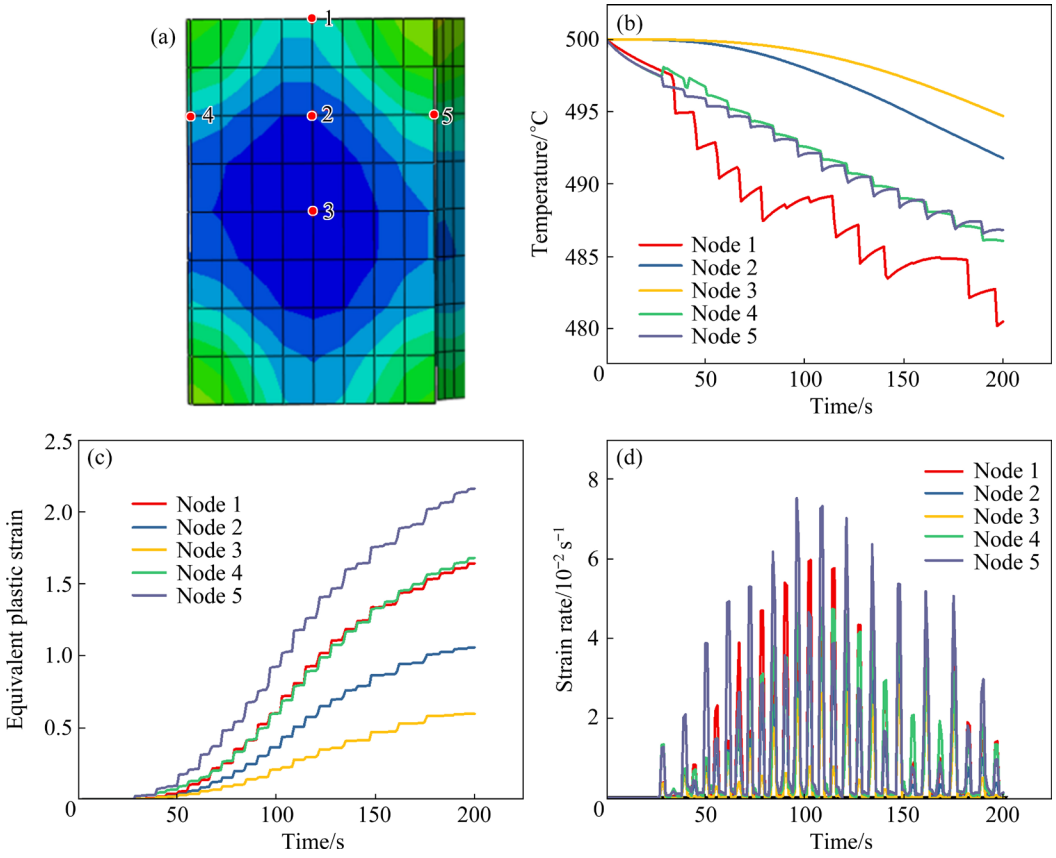

Fig. 1 Evolution of macroscopic specific parameters of selected nodes in whole hot ring rolling process: (a) Feature nodes selected from longitudinal section; (b) Temperature; (c) Equivalent plastic strain; (d) Strain rate

heat induced by the plastic deformation decreases with the proceeding of the rolling process due to the decreased radial feed velocity of the mandrel. The plastic heat production is smaller than the heat dissipation, thus resulting in the increased temperature drop at the center part.

As shown in Fig. 1, all the nodes have experienced 27 rolling passes in the hot rolling, and each pass only leads to small increment of the equivalent plastic strain. The distribution of the equivalent plastic strain is quite inhomogeneous and it decreases from edge surfaces to the center part of the cross section of the ring. Node 5 close to the mandrel exhibits the largest equivalent strain with the value of 2.16, which is larger than that of Node 4 close to the main roll. The radial feed is achieved by the movement of the mandrel and the edge surface close to the mandrel is subjected to severe strain compared to that on the surface close to the main roll. It can be seen that the overall strain rate is relatively low and it is less than 0.1 s^{-1}, indicating the limited feed velocity of the two rolling zones. The strain rate for different nodes is closely relative to the distribution of the equivalent plastic strain due to the constant linear velocity of the outer diameter of the ring blank.

3.1.2 Microstructure evolution analysis of CA model

As described in Section 2, the preparation of the ring blank consists of the casting and forging processes. The initial microstructure of the ring blank is the forged structure followed by the solution treatment, instead of the equiaxed grains of the casting state. The grain size is larger than 200 μm with the substructure and small recrystallized grains, as shown in Fig. 2. The initial microstructure mainly consists of the low-angle grain boundaries (LAGBs) with the fraction of 81.7%, and the average misorientation angle is 11.02°. The generation of the initial microstructure is made up of the formation of initial equiaxed grains and the dispersion of local subgrains, as shown in Fig. 3. The details of the steps for the generation of the initial microstructure are present in Ref. [31].

The microstructure evolution of Node 1 during multi-pass hot rolling is shown in Fig. 4. There is

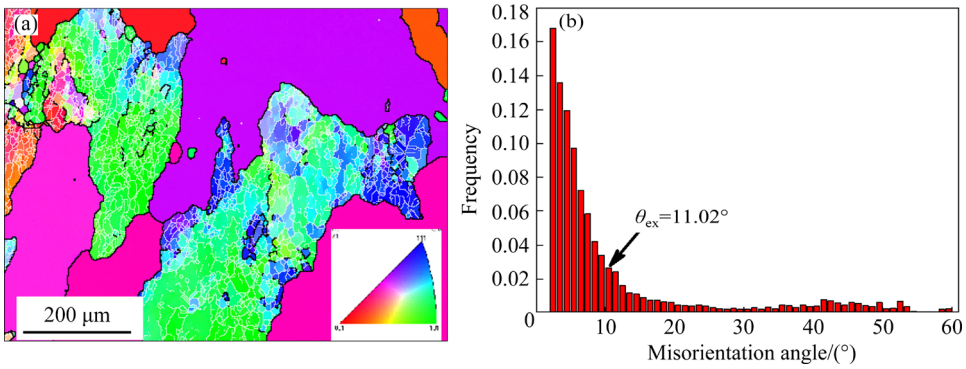

Fig. 2 Experimental initial microstructure (a) and misorientation distribution (b)

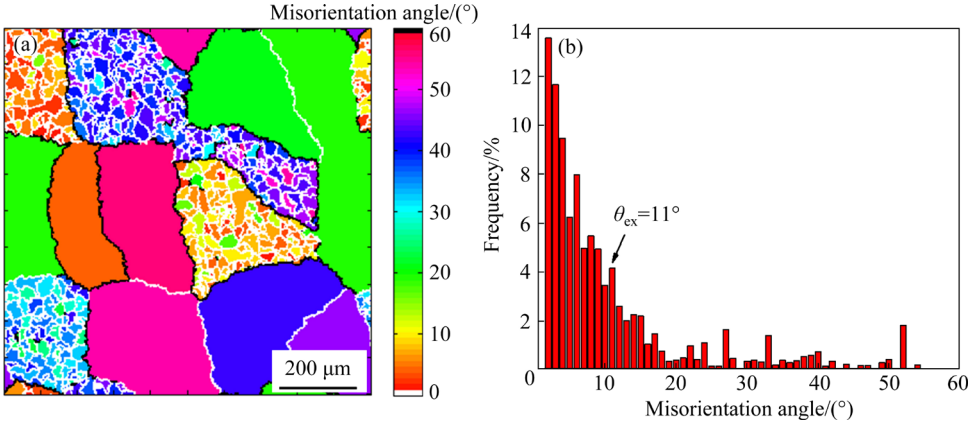

Fig. 3 CA simulated initial microstructure (a) and misorientation distribution (b)

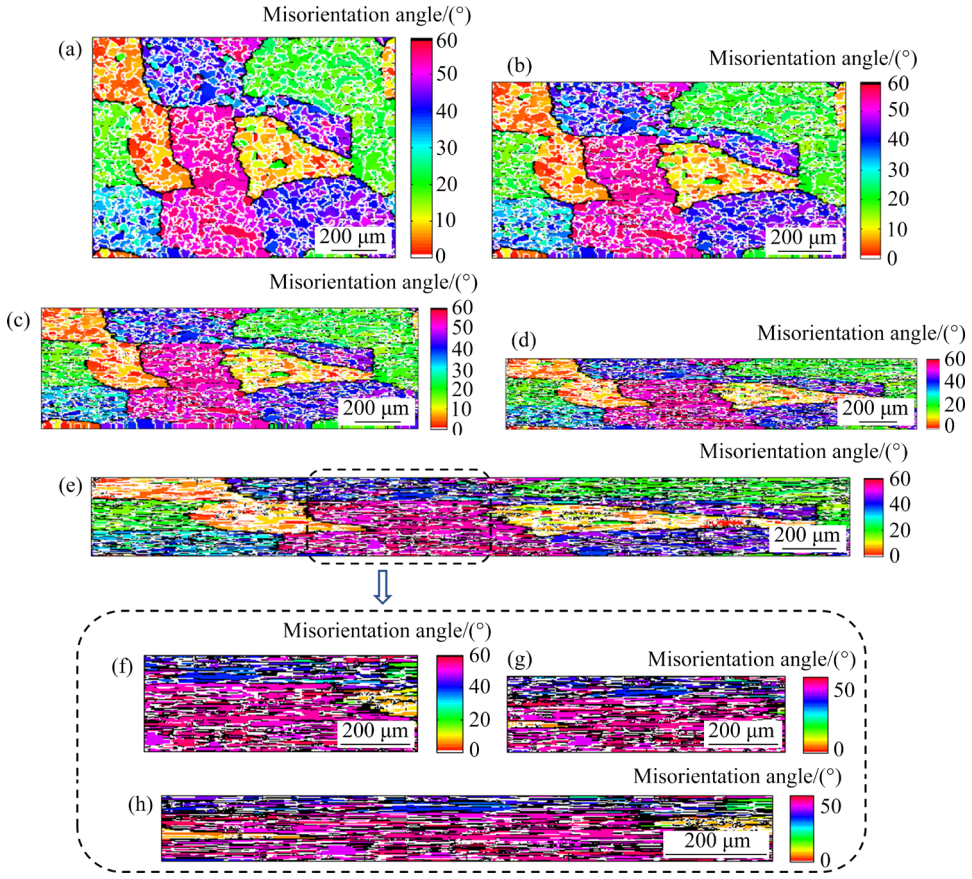

Fig. 4 Microstructure evolution of Node 1 at different rolling passes during hot ring rolling process: (a) Pass 6; (b) Pass 9; (c) Pass 12; (d) Pass 15; (e) Pass 18; (f) Pass 21; (g) Pass 24; (h) Pass 27

no obvious variation of the grain morphology after 6 passes as the equivalent plastic strain is smaller than the critical value for the recrystallization. The feed of the mandrel is small during the previous several passes and the dynamic/static recovery plays a vital role in the formation of the sub-grains with LAGBs. The equiaxed grains are compressed in the axial direction and elongated in the radial direction of the ring. Additionally, the LAGBs gradually transform into the high-angle grain boundaries (HAGBs) with the proceeding of the rolling passes. The HAGBs play a dominant role in the microstructure during the last several passes, indicating the obvious dynamic/static recrystallization at Node 1 during hot rolling process.

Similar to the distributions of the equivalent plastic strain and temperature, the recrystallization fraction and misorientation angle also show inhomogeneous distribution during the hot ring rolling process, as shown in Fig. 5. The recrystallization fraction is quite small during previously several passes and it increases with the increased rolling pass significantly. Node 5 shows sufficient recrystallization with the largest value of 91.9%, while it is 38.8% and 41.5% for Node 1 and Node 4, respectively. The distribution of the recrystallization fraction is similar to that of the equivalent plastic strain, indicating that the plastic strain is a key parameter for the variation of recrystallization fraction. The fraction of the LAGBs decreases with the increased rolling pass for all the nodes in the cross section, indicating that the CDRX plays a dominant role in the hot ring rolling process. The fraction of LAGBs at Node 5 decreases to 33.7% after the hot rolling process, while it is 72.7% for Node 3. The critical value of the HAGBs is 15° for aluminum alloy and the average misorientation angle exceeds 15° for all the nodes except Node 3. The average misorientation angle is 13.6° for Node 3, which accounts for the small recrystallization fraction. It can be found that recrystallization fraction starts to increase obviously when the average misorientation angle exceeds 15°, which is consistent with the critical condition for the onset of the CDRX process.

To analyze the microstructure uniformity in the cross section of the ring during hot rolling process, the CA simulated results at different nodes are shown in Fig. 6. It can be clearly seen that all the

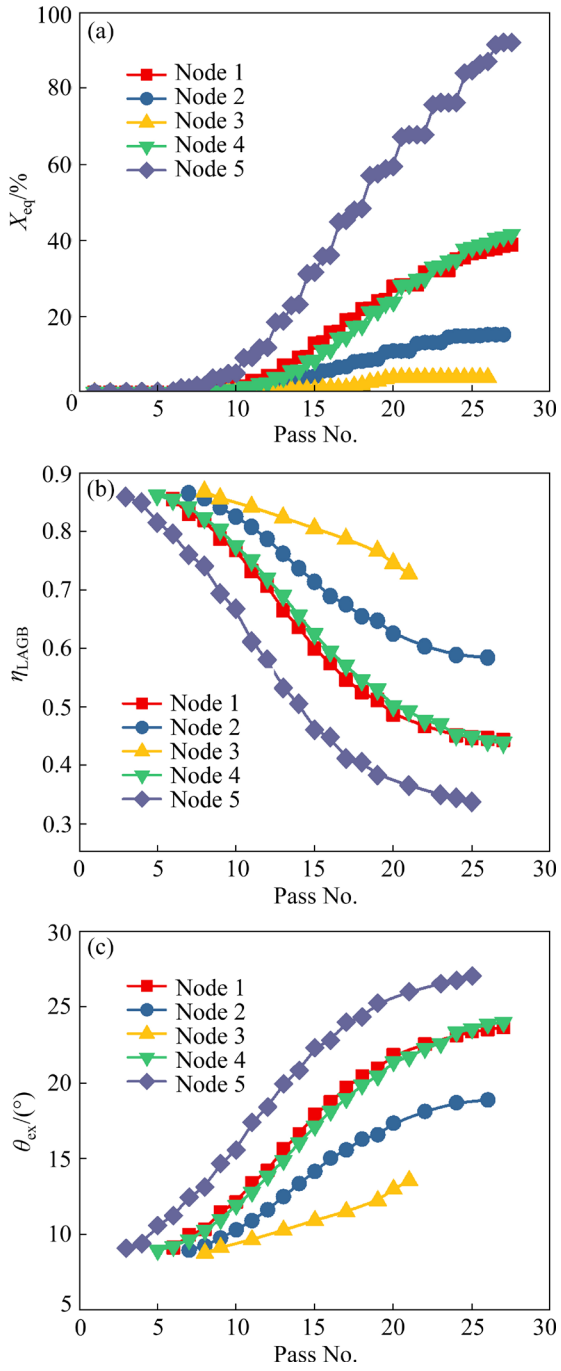

Fig. 5 Variation of microstructure parameters for each node (shown in Fig. 1(a)) in hot ring rolling process: (a) Recrystallization fraction (X_{eq}); (b) LAGBs fraction (η_{LAGB}); (c) Average misorientation angle (θ_{ex})

nodes present different characteristics in grain morphology and sub-structures ratio. Node 5 shows the most severe deformed grains with large fraction of HAGBs due to its large equivalent plastic strain. Node 1 and Node 4 also show obvious deformation with high fraction of HAGBs due to the contact with the main roll and the axial rolls. Nevertheless,

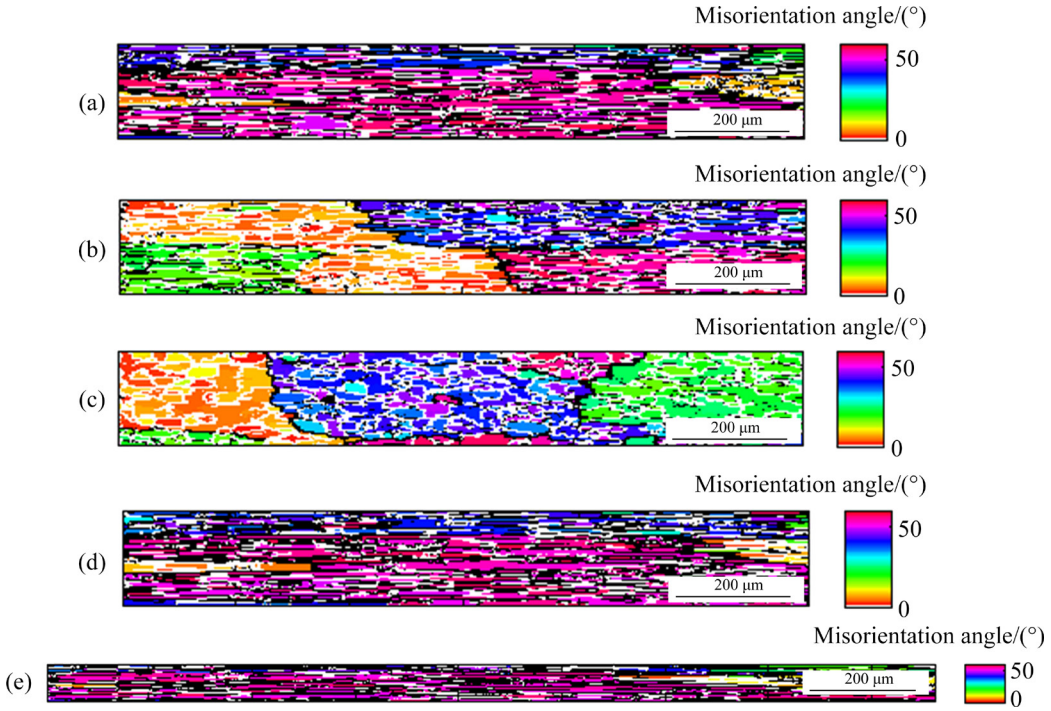

Fig. 6 Microstructure distribution at different nodes after hot ring rolling process: (a) Node 1; (b) Node 2; (c) Node 3; (d) Node 4; (e) Node 5

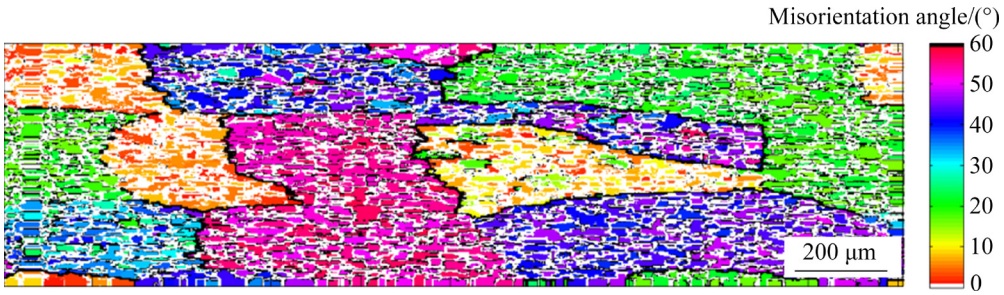

Fig. 7 Microstructure distribution at Node 2 after conventional ring rolling process

the grain morphology can be clearly seen at Node 2 and Node 3, and its LAGBs proportion is much higher than that of the nodes on the edge surface. It can be seen from Fig. 7 that the grain size in conventional ring rolling is much larger than that with two-stage hot and warm ring rolling. Meanwhile, the ratio of the grain length to grain height is much higher, indicating severe anisotropy of the microstructure.

The microstructure heterogeneity on the cross section of the ring is quantitatively analyzed in Fig. 8. The difference of the maximum equivalent recrystallization fraction is 88%, accompanied by the difference of maximum LAGBs ratio of 39%. Therefore, the anisotropy of the microstructure distribution is quite obvious during hot ring rolling process and it needs to be solved with a followed process.

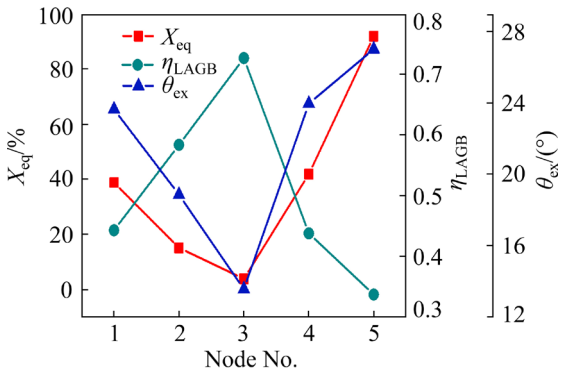

Fig. 8 Variation of microstructure parameters for different nodes after hot ring rolling process

3.2 Warm ring rolling and solution heat treatment in new forming process

3.2.1 Flow behavior analysis with FEM

Coarse grains with an elongated shape are

likely to appear in the final ring with conventional hot ring rolling, causing low ductility and significant anisotropy of tensile properties in the large rings. Fully equiaxed grains are beneficial to the improvement of the isotropy of the mechanical properties of the ring. Nevertheless, the coarse and elongated grains with substructures in conventional hot ring rolling weaken the strength and plasticity of the ring, as shown in Fig. 7.

In this work, warm ring rolling with the followed solution treatment is proposed to refine the grains. Figure 9 shows the inhomogeneous distributions of the temperature and the equivalent plastic strain during warm ring rolling, which are similar to those of the hot ring rolling. The temperature of the nodes on the edge surfaces decreases with fluctuations; while that of the nodes on the center part decrease smoothly. Different from that in hot ring rolling, the temperature of all nodes declines in a relatively slow rate and the temperature drop is smaller in warm ring rolling. The accumulated equivalent plastic strain is less than 1 with the total rolling passes of 71, which is much smaller than that in the hot ring rolling, as shown in Fig. 10. The radial feed of the mandrel in warm rolling is much smaller than that in the hot rolling due to the larger deformation resistance at lower temperature. The equivalent plastic strain of Node 3 is about 1/3 that of Node 1, indicating that the small radial feed of each pass results in significant difference of the plastic strain between the surfaces and the center part of the cross section. The overall strain rate is less than 0.017 s^{-1} and it is not beneficial to the accumulation of dislocation density and stored energy. The significant inhomogeneity of the strain distribution and low strain rate can affect the static recrystallization process, thus influencing the uniformity of the grains.

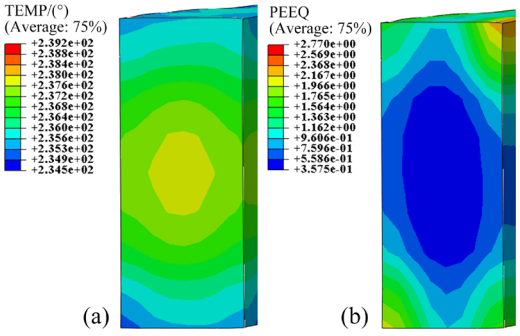

Fig. 9 Modeling of warm ring rolling process with FEM: (a) Temperature; (b) Equivalent plastic strain

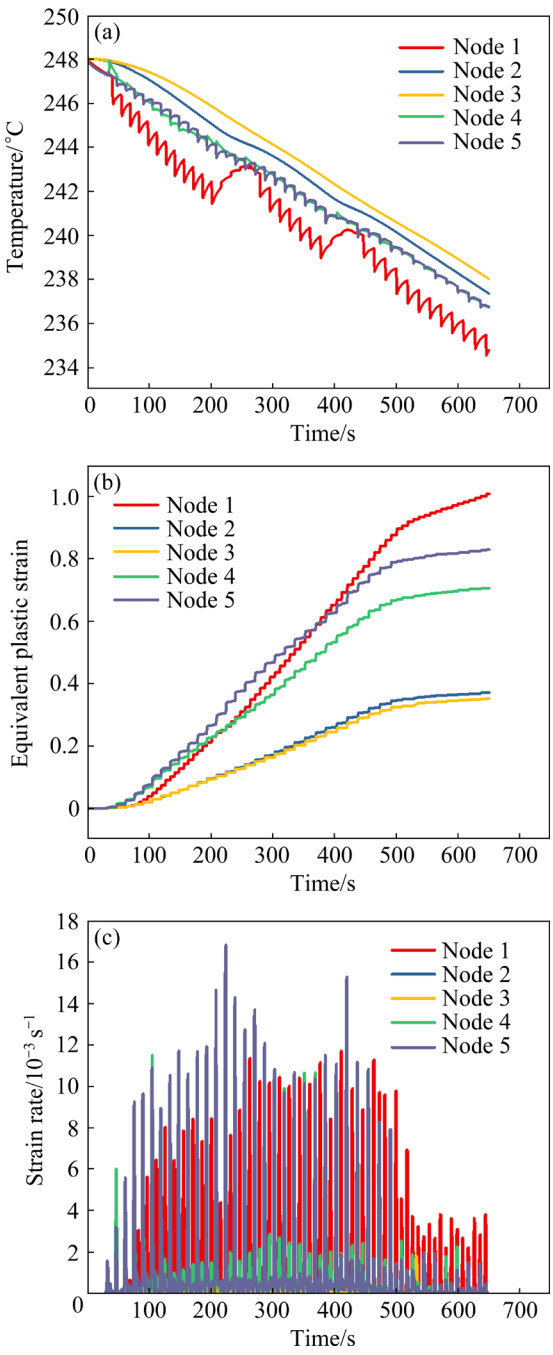

Fig. 10 Variations of temperature (a), equivalent plastic strain (b) and strain rate (c) of different nodes (shown in Fig. 1(a)) during warm ring rolling process

3.2.2 Microstructure distribution with warm rolling and solution treatment

Solution treatment is applied to the ring after the warm ring rolling, and the microstructure of different nodes is shown in Fig. 11. The elongated banded structures change to fully equiaxed grains with different sizes, indicating that complete static recrystallization has taken place for all nodes. The Node 1 shows the smallest average grain size with

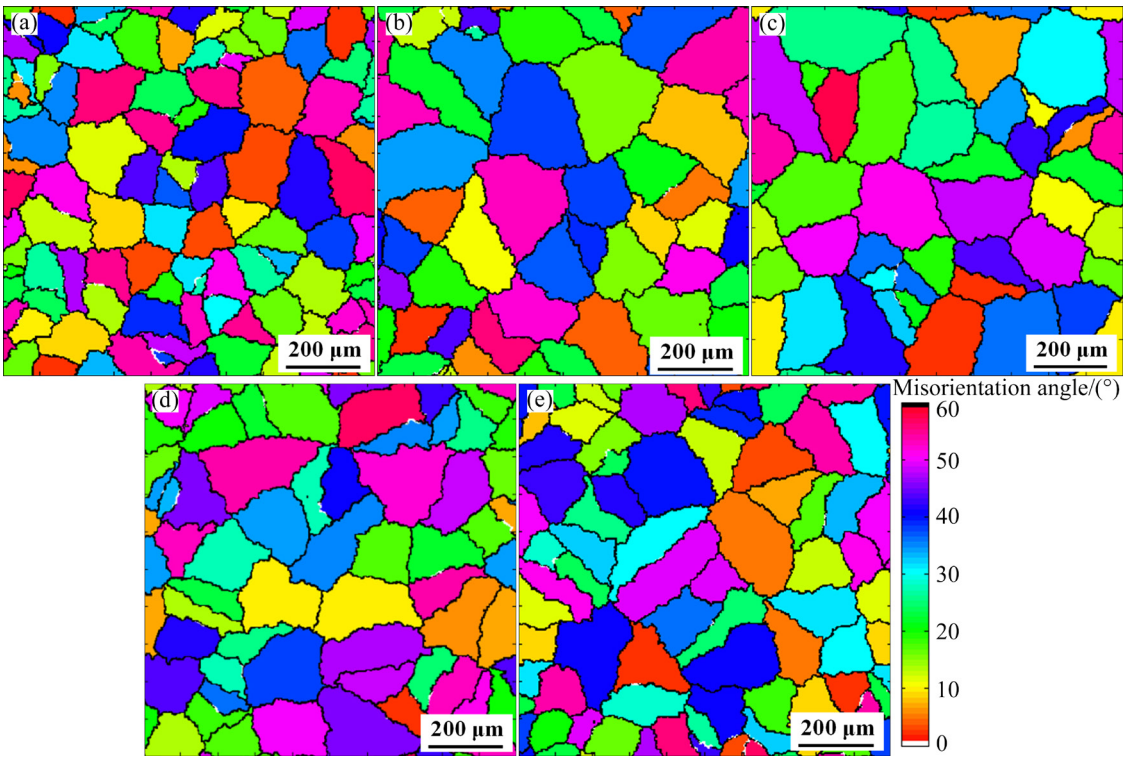

Fig. 11 Microstructure distribution at different nodes after warm ring rolling and solution treatment: (a) Node 1; (b) Node 2; (c) Node 3; (d) Node 4; (e) Node 5

121.7 μm, while it is 176.3 μm and 180.7 μm for Node 2 and Node 3, respectively. The deformation energy accumulating in the warm rolling process provides the driving force for the nucleation of the sub-grains and the grain refinement during the solution treatment. The difference of the equivalent plastic strain results in the inhomogeneous distribution of the grain size. Meanwhile, the strain rate during the warm rolling process is quite small due to the small feed of the mandrel; as a result, small strain rate is not beneficial to the large fraction of the SRX process and the sufficient grain refinement.

3.3 Experiment of ring rolling process

The engineering experiment of two-stage hot−warm ring rolling for AA2219 ring blank was conducted on a large radial−axial ring rolling mill. The initial ring blank was taken from the forged blank after horse frame reaming. The parameters of the ring rolling mill were consistent with those in Table 1. Firstly, the rollers were preheated to avoid the large temperature difference between the rollers and the ring blank. Then, the ring blank was heated to 500 °C in the trolley heating furnace with a holding time of 1 h. The hot ring rolling test was carried out and the ring blank was hot rolled into the thickness of 240 mm. The four rollers in the radial and axial deformation zones were sprayed and lubricated by the specified spray lubricant to suppress the rolling temperature rise during the hot ring rolling process. After hot rolling, the surface temperature and size of the hot ring blank were measured. When the temperature of the hot ring blank decreased to (240±5) °C, the warm ring rolling test was carried out immediately and the ring blank was warm rolled into the thickness of 180 mm. The size and the ovality of the ring were measured after the hot and warm ring rolling process. Finally, the warm rolled ring was solution-treated at 540 °C and held for 4 h. The microstructure and grain orientation at different positions of the ring were observed by the electron back scattered diffraction (EBSD) technique. After the solution treatment, the ring was artificial-aged at 165 °C and held for 23 h. Tensile coupons on the radial, axial and circular directions of the ring were extracted and the tensile test was conducted to investigate the mechanical properties of the ring with different forming technologies. The interval time between the solution and artificial aging process was smaller than 6 h to eliminate the effect

of the natural aging on the tensile properties.

The rolling force of the radial and axial deformation zones are calculated based on the recorded hydraulic pressure of the mandrel and upper cone rollers during the whole ring rolling process, as shown in Fig. 12. The average radial and axial rolling forces of the experimental hot rolling process are 3.062 and 1.339 MN, respectively, while the simulated values are 2.804 and 1.172 MN respectively, and the relative errors are 8.43% and 12.5%. For the warm ring rolling process, the average radial rolling force of stable rolling stage is 5.539 MN, while the simulated result is 5.036 MN with the error of 9.08%. The rolling force in warm rolling is much larger than that in hot rolling due to the larger resistance at lower temperature despite the relatively smaller equivalent strain. The axial rolling force in hot rolling is quite large due to the flatness of the obvious axial variation induced by the large radial feed, while it is small in warm rolling due to the small radial feed of the mandrel. The FE simulation of hot−warm ring rolling is verified to have a good agreement with the actual rolling forces.

Table 3 gives the temperature and geometric parameters of the hot and warm rolled ring. The simulated results agree with the experimental values with the average errors of 3%. The temperature of Node 5 is measured with the infrared camera and it is consistent with the simulated values. Ovality usually appears in the ring rolling process for the large-scale ring; however, it decreases significantly during the warm ring rolling process. The feed of the mandrel is quite small and the adjustment of the roundness can be achieved simultaneously in the warm rolling.

The rolled ring was solution-treated after the ring rolling processes. Then, the microstructure and grain orientation at different nodes of the cross section of the ring was observed by EBSD technique, as shown in Fig. 13 and Table 4. It can be observed that the total static recrystallization occurs at different positions of the cross section with few substructures. The initial large grains are refined effectively and its anisotropy as well as the grain texture induced by the forging or rolling processes is obviously decreased. The average grain size of the internal nodes is larger than that of the edge nodes with the size ranging from 118.3 to 182 μm, which is consistent with the simulated results. As a result, anisotropy of the microstructure distribution can be effectively decreased in the warm rolling with the followed solution treatment, which is difficult to be solved in the hot rolling

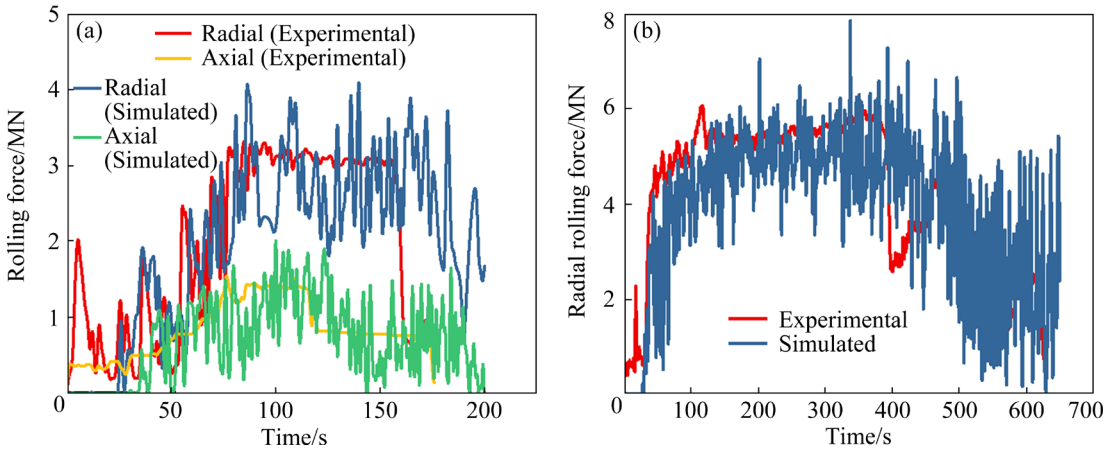

Fig. 12 Comparison between simulated and experimental rolling force: (a) Hot ring rolling; (b) Warm ring rolling

Table 3 Comparison between simulated and experimental results

Result	Hot ring rolling					Warm ring rolling				
	Diameter/mm	Ovality/mm	Height/mm	Width/mm	Temperature/°C	Diameter/mm	Ovality/mm	Height/mm	Width/mm	Temperature/°C
Experimental	4075	26	457	241	486.8	5051	3	450	180	235
Simulated	4070	36	459	247	488.4	5056	12	449	185	236
Error/%	0.123	−	0.438	2.49	0.329	0.1	−	0.222	2.778	0.426

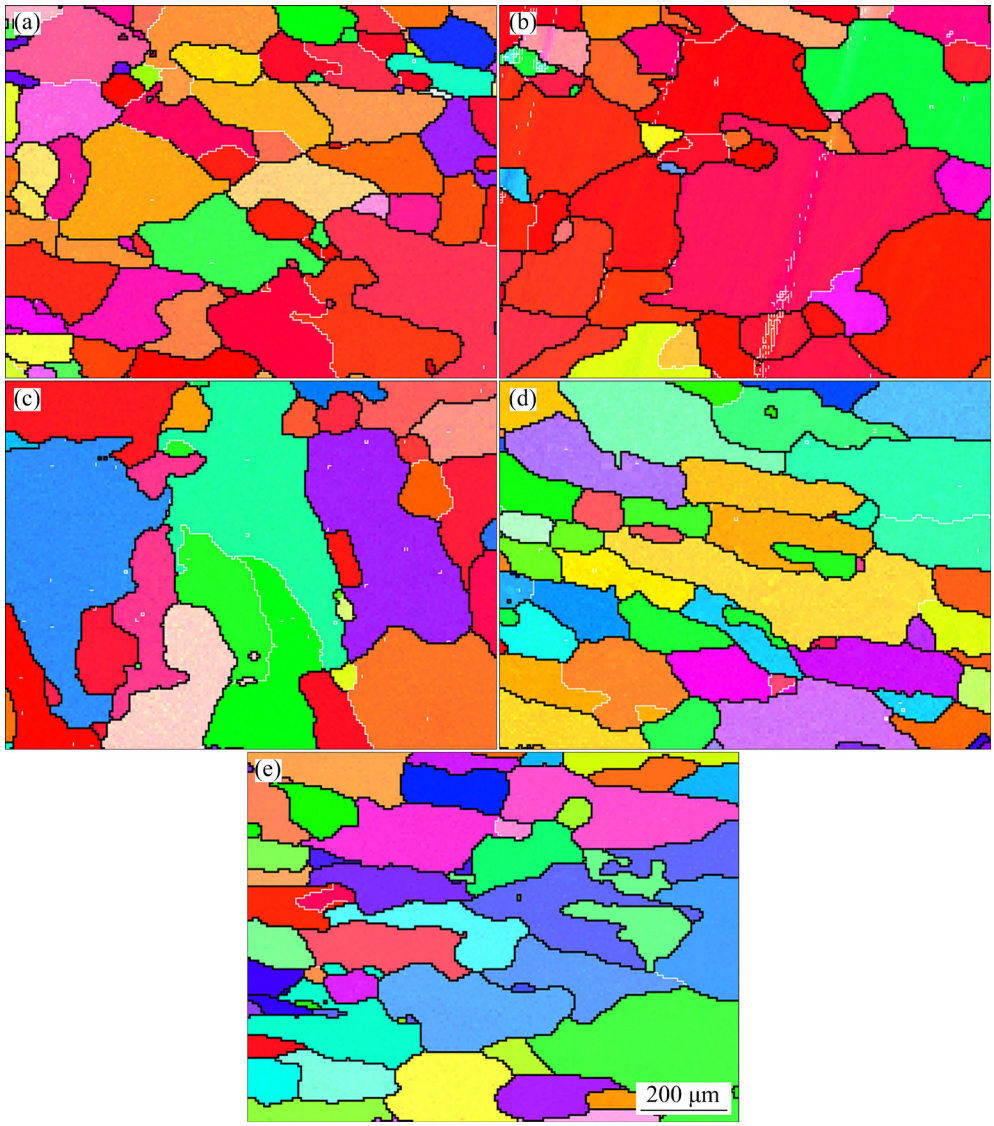

Fig. 13 Experimental average grain size at different nodes after warm ring rolling and solution treatment: (a) Node 1; (b) Node 2; (c) Node 3; (d) Node 4; (e) Node 5

Table 4 Comparison of simulated and experimental average grain size of different nodes of ring

Arerage grain size	Node No.				
	1	2	3	4	5
Experimental/μm	118.3	159.2	182.0	146	132.4
Simulated/μm	121.7	176.3	180.7	149.5	140.0
Error/%	5.4	10.7	0.7	2.4	5.7

process. The coupled multi-scale ring rolling simulation using FE+CA technique can be used to effectively simulate the macro/micro evolution of AA2219 in the hot−warm ring rolling process. Figure 14 shows the microstructure after the conventional hot ring rolling with deformation of 50% [6]. In the ring manufactured by the conventional process, grains are elongated along the circumferential direction, and some fine equiaxed recrystallized grains are observed near grain boundaries, as shown in Fig. 14(a). Coarse grains are obtained in the conventionally manufactured ring, with average grain size in the longitudinal plane of 385 μm after solution treatment. The longitudinal grains are extensively elongated along the circumferential direction and the aspect ratio of the grains (grain length/grain height) in the longitudinal plane reaches 9.7, showing significant elongated structure.

Figure 15 shows the stress−strain curves in different directions of the ring with conventional and new ring rolling process. The comparison of the tensile property with different forming technologies

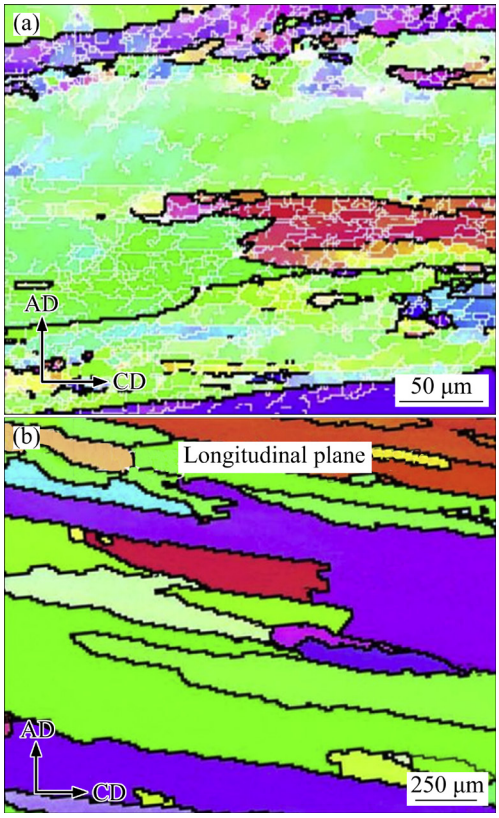

Fig. 14 Microstructure with conventional hot ring rolling: (a) After hot rolling with deformation of 50%; (b) After solution treatment [6]

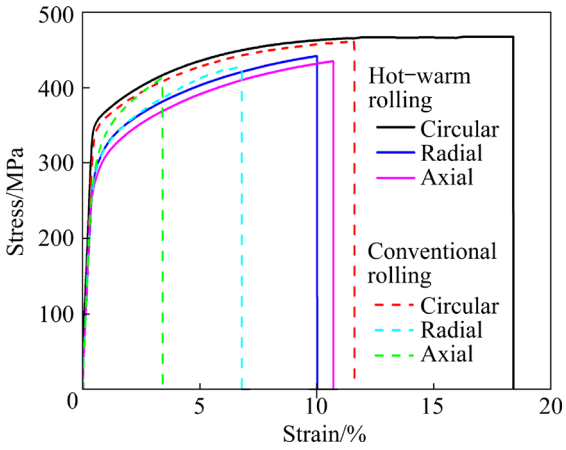

Fig. 15 Stress−strain curves in different directions of ring with conventional and new ring rolling process

is shown in Fig. 16. The ring blank prepared from the forging process is hot-rolled into the final ring component in the conventional ring rolling process. The UTS of the ring prepared by conventional ring rolling ranges from 413 to 462 MPa, and YS changes from 324 to 339 MPa. Nevertheless, the elongation in the axial and radial directions is much smaller than that in the circular direction, which cannot meet the requirements of the properties in the aerospace. After applying the warm ring rolling followed by solution treatment, the UTS and YS both increase compared to those in the conventional ring rolling. Furthermore, the elongation in all directions significantly increases and the isotropy of the plasticity is greatly improved, which exceeds the requirements of the aerospace ring component.

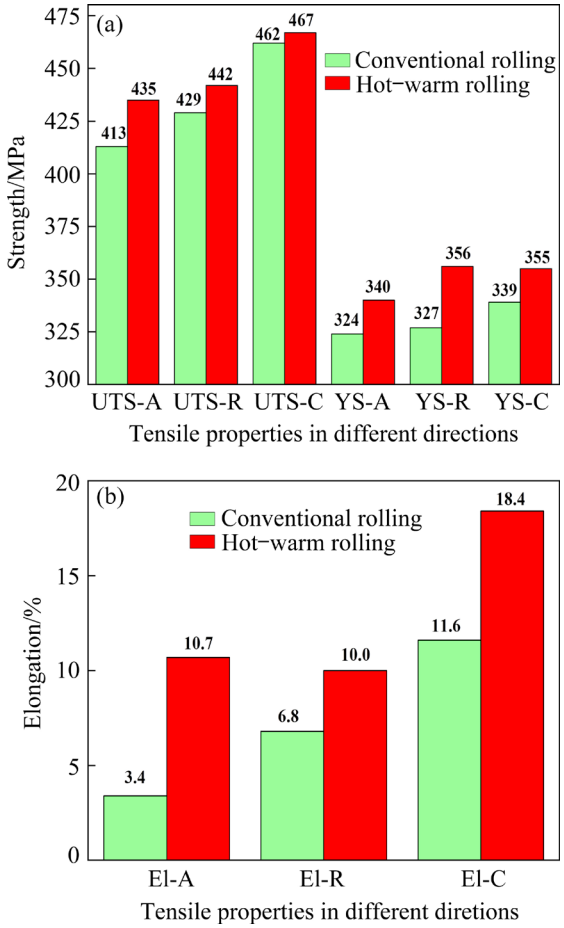

Fig. 16 Comparison of tensile properties with different forming technologies (UTS, YS and El mean ultimate tensile strength, yield strength and elongation; A, R and C mean axial, radial and circular direction of the ring)

To qualitatively describe the anisotropy of the tensile properties in different directions of the ring with different forming technologies, an anisotropy coefficient of tensile properties, ω, is defined in Eqs. (16) and (17). The anisotropy coefficient of UTS decreases to 7.1% with the new technology in this study compared to that of 11.3% with conventional hot rolling, while the anisotropy coefficient of YS hardly changes, as given in Table 5. There is significant difference of the elongation in the axial and circular direction of the

ring with conventional hot rolling, resulting in an anisotropy coefficient of 112.8%. The elongation in the axial direction obviously increases with the hot−warm rolling process, and as a result, the anisotropy coefficient of elongation decreases to 64.5%. It can be concluded that the warm ring rolling followed by solution treatment is beneficial to increasing the elongation and improving the isotropy of the mechanical properties accompanied by the increase of the strengths.

$$\omega=(\Omega_1-\Omega_3)/\Omega_m\times100\% \quad (16)$$

$$\Omega_m=(\Omega_1+\Omega_2+\Omega_3)/3 \quad (17)$$

where Ω_1, Ω_2 and Ω_3 are the maximum, medium and minimum values of the tensile properties of the three directions of the ring, and Ω_m is the average value of the tensile properties of the three directions of the ring.

Table 5 Anisotropy coefficient of tensile properties with different forming technologies

Forming technology	Anisotropy coefficient/%		
	UTS	YS	Elongation
Conventional ring rolling	11.3	4.5	112.8
Hot−warm ring rolling	7.1	4.3	64.5

4 Conclusions

(1) The CA method includes the models of dislocation density, nucleation rate, grain boundary migration and topological deformation.

(2) Both the hot and warm ring rolling processes show inhomogeneous distribution of the equivalent strain. The temperature of the edge nodes decreases with repeated fluctuation while that of the core nodes decrease smoothly with the proceeding of the rolling passes. The temperature declines in a relatively slow rate and the temperature drop is smaller in warm ring rolling.

(3) The grains of the edge nodes are elongated with the increased fraction of high-angle grain boundaries in rolling process. The fraction of CDRX increases with the increased rolling pass through the transformation of LAGBs to HAGBs. The banded structures formed during the rolling process change to equiaxed grains during the solution treatment.

(4) The new forming technology significantly increases the tensile properties in all directions of the ring, especially for the elongation. The isotropy of the tensile properties is obviously improved with the new forming technology.

(5) The multi-scale simulated results agree with the experiment and the coupled FEM−CA models provide guidance for the flow behavior and microstructure evolution.

Acknowledgments

The authors are grateful for the financial supports from the National Natural Science Foundation of China (Nos. 51705248, 52005517), the State Key Laboratory for High-Performance Complex Manufacturing, Central South University, China (No. ZZYJKT2021-05), Key Research and Development Plan of Heilongjiang Province, China (No. GA21D003), and the Natural Science Foundation of Hunan Province, China (No. 2020JJ4703).

References

[1] JIN Peng, LIU Yi-bo, LI Fu-xiang, LI Jun-zhao, SUN Qing-jie. Realization of structural evolution in grain boundary, solute redistribution and improved mechanical properties by adding TiC nps in wire and arc additive manufacturing 2219 aluminium alloy [J]. Journal of Materials Research and Technology, 2021, 11: 834−848.

[2] GUO Wan-fu, HE Hai-lin, YI You-ping, HUANG Shi-quan, MAO Xian-chang, FANG Jie, HUANG Jian-wu. Effects of axial cold-compression on microstructure uniformity and mechanical property enhancement of large 2219 Al−Cu alloy rings [J]. Materials Science and Engineering A, 2020, 798(12): 140233.

[3] HE Hai-lin, YI You-ping, HUANG Shi-quan, ZHANG Yu-xin. An improved process for grain refinement of large 2219 Al alloy rings and its influence on mechanical properties [J]. Journal of Materials Science & Technology, 2019, 35: 55−63.

[4] LIANG Lei, GUO Liang-gang, WANG Yi-fan, LI Xue-chao. Towards an intelligent FE simulation for real-time temperature-controlled radial-axial ring rolling process [J]. Journal of Manufacturing Processes, 2019, 48: 1−11.

[5] GUO Liang-gang, YANG He. Numerical simulation of inhomogeneous deformation in cold ring rolling [J]. Steel Research International, 2010, 81(9): 198−201.

[6] HE Hai-lin, YI You-ping, CUI Jin-dong, HUANG Shi-quan. Hot deformation characteristics and processing parameter optimization of 2219 Al alloy using constitutive equation and processing map [J]. Vacuum, 2019, 160: 293−302.

[7] SHARMA V, KUMAR K S, RAO B N, PATHAK S D. Effect of microstructure and strength on the fracture behavior of AA2219 alloy [J]. Materials Science and Engineering A, 2009, 502: 45−53.

[8] TANG Xue-feng, WANG Bao-yu, ZHANG Hua, FU Xiao-bin, JI Hong-chao. Study on the microstructure evolution during radial-axial ring rolling of IN718 using a unified internal state variable material model [J]. International Journal of Mechanical Sciences, 2017, 128/129: 235−252.

[9] KAZEMI-NAVA E E A, JAMAATI R, AVAL H J. Effect of single roll drive cross rolling on the microstructure, crystallographic texture, and mechanical behavior of Al−Zn−Mg−Cu alloy [J]. Archives of Civil and Mechanical Engineering, 2022, 22: 41.

[10] LI Xue-chao, GUO Liang-gang, LIANG Lei, YANG Wen-rong. Motion control of guide rolls in intelligent simulation for profiled ring rolling process [J]. Procedia Manufacturing, 2018, 15: 97−104.

[11] LIU Xiao, LI Luo-xing, HE Feng-yi, ZHOU Jia, ZHU Bi-wu, ZHANG Li-qiang. Simulation on dynamic recrystallization behavior of AZ31 magnesium alloy using cellular automaton method coupling Laasraoui–Jonas model [J]. Transactions of Nonferrous Metals Society of China, 2013, 23: 2692−2699.

[12] WANG C, GEIJAELAERS H J M, OMERSPAHIC E, RECINA V, BOOGAARD A H. Influence of ring growth rate on damage development in hot ring rolling [J]. Journal of Materials Processing Technology, 2016, 227: 268−280.

[13] HAN Xing-hui, HUA Lin, ZHOU Guang-hua, LU Bo-han, Wang Xiao-kai. A new cylindrical ring rolling technology for manufacturing thin-walled cylindrical ring [J]. International Journal of Mechanical Sciences, 2014, 81: 95−108.

[14] HAN Xing-hui, HUA Lin. Effect of friction on combined radial and axial ring rolling process [J]. Tribology International, 2014, 73(5): 117−127.

[15] ZHU Xing-lin, LIU Dong, YANG Yan-hui, HU Yang, ZHENG Yong. Optimization on cooperative feed strategy for radial–axial ring rolling process of Inco718 alloy by RSM and FEM [J]. Chinese Journal of Aeronautics, 2016, 29: 831−842.

[16] LIANG Lei, GUO Liang-gang, LI Xue-chao, YANG Wen-rong. Intelligent simulation for real-timely force-controlled radial-axial rolling process of supersized aluminium alloy rings [J]. Procedia Manufacturing, 2018, 15: 105−112.

[17] ZHANG Tao, LU Shi-hong, WU Yun-xin, GONG Hai. Optimization of deformation parameters of dynamic recrystallization for 7055 aluminum alloy by cellular automaton [J]. Transactions of Nonferrous Metals Society of China, 2017, 27: 1327−1337.

[18] ZHANG Fu-xiang, LIU Dong, YANG Yan-hui, LIU Cui-xia, ZHANG Zhe, WANG Hai, WANG Jian-guo. Investigation on the meta-dynamic recrystallization behavior of Inconel 718 superalloy in the presence of δ phase through a modified cellular automaton model [J]. Journal of Alloys and Compounds, 2020, 817: 152773.

[19] LIN Yong-cheng, LIU Yan-xing, CHEN Ming-song, HUANG Ming-hui, MA Xiang, LONG Zhi-li. Study of static recrystallization behavior in hot deformed Ni-based superalloy using cellular automaton model [J]. Materials & Design, 2016, 99: 107−114.

[20] MADEJ L, SIERADZKI L, SITKO M, PERZYNSKI K, RADWANSKI K, KUZIAK R. Multi scale cellular automata and finite element based model for cold deformation and annealing of a ferritic–pearlitic microstructure [J]. Computational Materials Science, 2013, 77: 172−181.

[21] BAKHTIARI M, SALEHI M S. Reconstruction of deformed microstructure using cellular automata method [J]. Computational Materials Science, 2018, 149: 1−13.

[22] LEE H W, IM Y T. Numerical modeling of dynamic recrystallization during nonisothermal hot compression by cellular automata and finite element analysis [J]. International Journal of Mechanical Sciences, 2010, 52: 1277−1289.

[23] JIN Zhao-yang, LIU Juan, CUI Zhen-shan, WEI Dong-lai. Identification of nucleation parameter for cellular automaton model of dynamic recrystallization [J]. Transactions of Nonferrous Metals Society of China, 2010, 20: 458−464.

[24] YANG Zi-you, JIN Kang-ning, FANG Hui, HE Jin-shan. Multi-scale simulation of solidification behavior and microstructure evolution during vacuum electron beam welding of Al−Cu alloy [J]. International Journal of Heat and Mass Transfer, 2021, 172: 121156.

[25] ZHANG Tao, LI Lei, LU Shi-hong, ZHANG Jia-bin, GONH Hai. Comparisons of flow behavior characteristics and microstructure between asymmetrical shear rolling and symmetrical rolling by macro/micro coupling simulation [J]. Journal of Computational Science, 2018, 29: 142−152.

[26] ZHENG Cheng-wu, XIAO Na-min, LI Dian-zhong, LI Yi-yi. Microstructure prediction of the austenite recrystallization during multi-pass steel strip hot rolling: A cellular automaton modeling [J]. Computational Materials Science, 2008, 44: 507−514.

[27] LIU Lei, WU Yun-xin, GONG Hai, LI Shuang, AHMAD A S. A physically based constitutive model and continuous dynamic recrystallization behavior analysis of 2219 aluminum alloy during hot deformation process [J]. Materials, 2018, 11(8): 1443.

[28] LIU Lei, WU Yun-xin, GONG Hai, WANG Kai. Modification of constitutive model and evolution of activation energy on 2219 aluminum alloy during warm deformation process [J]. Transactions of Nonferrous Metals Society of China, 2019, 29: 448−459.

[29] MOON C, THUILLIER S, LEE J, LEE M. Mechanical properties of solution heat treated Al−Zn−Mg−Cu (7075) alloy under different cooling conditions: analysis with full field measurement and finite element modeling [J]. Journal of Alloys and Compounds, 2021, 856: 158180.

[30] DING R, GUO Z X. Coupled quantitative simulation of microstructural evolution and plastic flow during dynamic recrystallization [J]. Acta Materialia, 2001, 49: 3163−3175.

[31] LIU Lei, WU Yun-xin, AHMAD A S. A novel simulation of continuous dynamic recrystallization process for 2219 aluminium alloy using cellular automata technique [J]. Materials Science and Engineering A, 2021, 815: 141256.

2219 铝合金环轧过程流变行为及组织演变多尺度数值仿真

董 方[1,2]，张 涛[1,2]，吴运新[1,2]，刘 磊[1,2]，郝铁文[1,2,3]

1. 中南大学 轻合金研究院，长沙 410083；
2. 中南大学 高性能复杂制造国家重点实验室，长沙 410083；
3. 一重集团大连工程技术有限公司，大连 116600

摘 要：开展 2219 铝合金环轧过程流变行为和显微组织演变的多尺度数值仿真。提出一种与传统热轧成形不同的新环轧技术，包括两阶段的热轧−温轧变形。结果表明，环件截面的温度、应变和应变速率呈现不均匀分布。边部节点大应变使得其内部晶粒被拉长，随着轧制过程的进行，小角度晶界逐渐转变为大角度晶界，使得再结晶百分数提高。固溶处理将轧制变形中拉长的带状组织转变为等轴晶组织，使材料发生完全静态再结晶。不均匀的温度和应变分布使得截面显微组织分布不均匀。通过环轧工艺试验，分析轧制过程中轧制力和环件几何尺寸变化规律。采用提出的新工艺，环件各方向力学性能和各向同性显著提升，尤其是伸长率提升显著。

关键词：2219 铝合金；两阶段热−温环轧；显微组织仿真；再结晶；拉伸性能

(Edited by Bing YANG)